

Observations with the Southern Connecticut Stellar Interferometer. II. First Three-Telescope Observations and a New Diameter Measurement of Arcturus

ELLIOTT P. HORCH ,^{1,*} SEBASTIAN M. LUCERO,¹ MAX MARTONE ,¹ RILEY C. BARRETT,¹ ANA I. BACULIMA DURÁN ,¹ FIONA T. POWERS ÖZYURT ,¹ GAGE POSICK ,¹ ALEXANDER PETROSKI ,¹ JAMES W. DAVIDSON, JR. ,² STEVEN R. MAJEWSKI ,² RICHARD A. PELLEGRINO ,³ PAUL M. KLAUCKE,^{1,†} XAVIER LESLEY-SALDAÑA ,^{1,‡} TORRIE SUTHERLAND ,^{1,§} AND OLIVIA S. WEISS ,^{1,¶}

¹Department of Physics, Southern Connecticut State University, 501 Crescent Street, New Haven, CT 06515, USA

²Department of Astronomy, University of Virginia, 530 McCormick Road, Charlottesville, VA 22904, USA

³CSCU Center for Quantum and Nanotechnology, Southern Connecticut State University, 501 Crescent Street, New Haven, CT 06515, USA

ABSTRACT

We discuss the most recent observations made with the Southern Connecticut Stellar Interferometer (SCSI), which is a three-station stellar intensity interferometer located on the campus of Southern Connecticut State University, in New Haven, Connecticut. Two different kinds of observations are presented. We first analyze observations of Vega taken in a three-telescope mode. (Previously, the instrument had only two operational stations.) We show that, while the efficiency remains nearly identical to that reported in our last paper, the addition of the third station allows more photon data to be recorded simultaneously, and therefore we can build up the photon-bunching peak in the data stream in fewer hours on sky for an unresolved source. In the second part of the paper, we report our observations to date of the nearby red giant star, Arcturus, most of which occurred in the first half of 2025. These show that, as a partially resolved source at the baselines we used, we detect fewer correlations in the photon-bunching peak than for an unresolved source of comparable brightness. Combining the data with speckle imaging observations taken at Apache Point Observatory, we derive a new measurement of Arcturus' diameter that extends the time baseline of interferometric observations of the star and is consistent with previous analyses made by other investigators.

Keywords: Astronomical instrumentation (799) — Interferometers (805) — Field stars (2103) — Stellar radii (1626)

1. INTRODUCTION

Stellar intensity interferometry (SII), which was first discussed by R. H. Brown & R. Q. Twiss (1956, 1958), is a technique used for deriving extremely high-resolution information of astronomical sources without the need of interfering the light from different stations. Instead, correlated intensity variations are observed when the frequency bandwidth of the light detected is narrow enough to reveal non-Poissonian fluctuations in the photon flux received at each telescope, known as the Hanbury Brown and Twiss (HBT) effect, or, in the photon counting regime, photon bunching. The degree of correlation observed at a given baseline can then be used to infer a Fourier component of the spatial distribution of the source, in other words, to make a visibility measurement. For visible light, the degree of correlation is usually very small, and so what limits the technique is the signal-to-noise ratio that is achievable; nonetheless, Hanbury Brown and his collaborators succeeded in building a two-station interferometer with very large telescopes. Details of the astronomical observations done with this instrument appear in R. Hanbury Brown et al. (1974). Even with the large size of the collecting apertures, the instrument was only capable of making diameter measurements of very bright

Email: horche2@southernct.edu

* Adjunct Astronomer, Lowell Observatory.

† Current address: Department of Physical and Life Sciences, Quinnipiac University, 275 Mount Carmel Avenue, Hamden, CT 06518

‡ Current address: Department of Astronomy, The Ohio State University, 140 West 18th Avenue, Columbus, OH 43210, USA

§ Current address: Apache Point Observatory, P.O. Box 59, Sunspot, NM 88349-0059

¶ Current address: Lowell Observatory, 1400 West Mars Hill Road, Flagstaff, AZ 86001

stars, ostensibly due to the timing precision of the photomultiplier tubes and electronics available at the time. Because of this, SII fell out of favor as the technical feasibility of high-precision optical metrology was realized and the research behind the current generation of long baseline optical interferometers in astronomy gained momentum in the 1980's.

However, there is a renewed and growing interest in SII today, and several groups have successfully revived and improved the technique with modern instrumentation. Generally, the systems used in these projects have fallen into two very different categories. In the first category, large telescopes that do not have optical-grade image quality are used, and the light is focused into a relatively large spot ($\sim 1\text{cm}$ in diameter), where it strikes a photomultiplier tube (PMT) and is read out there. These are in effect a repurposing of Imaging Atmospheric Cherenkov Telescopes (IACTs) for periods when the Moon is too bright to observe Cherenkov radiation from energetic particles entering the atmosphere. This approach is similar to the approach of Hanbury Brown and Twiss, but with the advantage of modern photomultiplier tubes, which have substantially higher quantum efficiencies and better timing characteristics than those of the 1970's. The Very Energetic Radiation Imaging Telescope Array System (VERITAS) (A. U. Abeysekara et al. 2020), the Major Atmospheric Gamma-Ray Imaging Cherenkov (MAGIC) array (V. A. Acciari et al. 2020), and High Energy Stereoscopic System (H.E.S.S.) (A. Zmija et al. 2024) are examples of this type of system. The other approach, which includes the Arizona State University Stellar Intensity Interferometer (ASUSII) (T. J. Mozdzen et al. 2025), the Nice Observatory system (J.-P. Rivet et al. 2018), the Asiago Observatory system (L. Zampieri et al. 2021), and our own work (E. P. Horch et al. 2022), hereafter Paper I, is to use smaller telescopes that deliver true optical quality, and to focus the relatively small spot of light onto a very fast detector, typically a single-photon avalanche diode (SPAD) detector with timing jitter of less than 100 ps.

Most recently, some of these groups have gone beyond the detection of photon bunching to making increasingly high-precision measurements of stars. J.-P. Rivet et al. (2020) presented an analysis of P Cyg where SII data was combined with high-resolution spectroscopy to infer the distance to the star; the result was 1.56 ± 0.25 kpc, which is comparable in precision to *Gaia*. Both E. S. G. de Almeida et al. (2022) and N. Matthews et al. (2023) followed that work with studies of γ Cas and Rigel. A. Acharyya et al. (2024) measured the diameter of β UMa at visible wavelengths for the first time, obtaining a precision of roughly 5%, A. Archer et al. (2025) has recently measured the oblateness of γ Cas, also to a few percent, and N. Vogel et al. (2025) detail new measurements of the diameters of four stars (β Cru, η Cen, σ Sco, and δ Sco) with uncertainties ranging from 2 to 8%. These results, while not yet as precise as what is currently possible with Michelson-style long baseline optical interferometers, nonetheless show the potential of the modern SII today. This has in turn spurred on investigations to improve efficiency in such systems, examples of which include S. Tolila et al. (2024), V. G. Leopold et al. (2025), S. Karl et al. (2025), N. Matthews et al. (2025), and J. Cortina et al. (2025).

In the present study, we build upon the work in our Paper I to do two things. First, we detect the HBT signal with SCSI using three telescopes for the first time, allowing us to refine our understanding of the instrument performance. We then describe SCSI observations of Arcturus ($= \alpha$ Boo, HR 5340, HIP 69673), which show partial correlation at baselines of 2-3 m. Combining with speckle observations taken with the Differential Speckle Survey Instrument (DSSI) at Apache Point Observatory, we are able make a new diameter measurement of the star. We discuss this result in light of previous work.

2. THREE-TELESCOPE OPERATIONS

2.1. *Instrumentation and Observing Method*

In Paper I, we describe our instrumentation and the observing process for a two-telescope arrangement. The main components used in this mode are (1) two 61-cm portable Dobsonian telescopes made by Equatorial Platforms, (2) MicroPhotonDevices PDM Series SPAD detectors, and (3) a PicoQuant PicoHarp 300 timing module. The SPAD detectors are connected to an optical harness that contains a collimating lens, the narrow bandpass filter (usually 532 nm with a full width at half maximum [FWHM] of 1.2 nm) and a reimaging lens that focuses the light onto the detector. This detector package is then mounted at the Newtonian focus of each telescope, and signal wires are connected from the SPADs to the two input channels of the timing module. The PicoHarp has the ability to timestamp the detected photons with a precision of 4 ps; the detector timing jitter, however, results in cross-correlation timing precision of ~ 50 ps, and so, as described in Paper I, we typically bin the data into 64-ps bins in order to identify correlation peaks. In this case, the HBT peak is effectively a small delta function sitting on top of the constant pedestal of random correlations in the timing cross-correlation function made from the photon timings recorded at each station.

In the three-telescope observations presented here, a third identical telescope and detector are added to the set-up, and we use an 8-channel correlator, the PicoQuant HydraHarp 400 (where five of the eight available channels are not used). The HydraHarp can time stamp events to 1 ps, and again, this is much higher than the detector timing jitter. Telescopes 1 and 2 were set up in exactly the same way as in Paper I; they were aligned in a north-south direction with Telescope 2 north of Telescope 1, based on paint spots on the asphalt at the observing location that were originally marked by observing the shadow cast by a plumb bob at solar noon several years ago and repainted twice since then. Telescope 3 was then set up west of Telescope 1, so that the locations of the telescopes were at the vertices of a right triangle (with Telescope 1 at the apex of the 90-degree angle). The legs of the right triangle were then nominally along the north-south and east-west directions, and the hypotenuse was represented by the baseline between Telescopes 2 and 3. Generally, we tried to place Telescope 3 in a position where the east-west baseline was approximately the same length as the north-south baseline. The placement of Telescope 3 was aided by long wooden beams that could easily be placed on the asphalt in orthogonal directions. These were laid along both the north-south paint spots and in the orthogonal direction. For each observing session, photographs were taken of the arrangement so that, if there were significant deviations from the north-south and east-west directions, these could be estimated from these images. The length of the north-south and east-west baselines was measured with a tape measure, using identical fiducial positions on each telescope.

Once the telescopes were placed and their positions documented, observing proceeded by first checking the collimation of each telescope with a laser collimator and then performing pointing alignments on two bright stars separated on the sky by at least 30 degrees, after which the telescopes would track. We then place the SPAD detectors at the focal point, and whenever possible, we would first point toward a planet (usually Jupiter or Mars) to align the finder telescopes and the detectors. Because the detectors have a very small active area (a diameter of 100 microns) and are not perfectly aligned with the optical axis, the technique of using an extended object allows us to quickly adjust the finder to an approximate match to the detector position in the field of view. Once roughly aligned, we would point to the science target and attempt to maximize the count rate on each detector. When counts were maximized at all telescopes, we took data in five-minute files, with an observer manually guiding each telescope throughout to keep the count rate as high as possible. (In five minutes, the shift of the cross-correlation peak within the data file was typically of the order of one 64-ps bin, and without manual guiding, we find that stars often slide off the detector in 10 to 30 seconds due to imperfect tracking.) Thus, in 3-telescope mode, an observing team of at least four people is needed, one to guide at each telescope, and a fourth person to manage the data collection process.

In order to process the data correctly, two types of calibration measurements are important. These are (1) estimates of height differences between the telescopes as a function of position, and (2) signal timing differences due to slight differences in cable length and intrinsic differences in the timing that can be measured between the channels of the timing correlators we use. For height differences, we use a spirit level starting at the location of Telescope 1 and then build up the (differential) topology of the site by placing the level at different places in a raster sequence over the area used for our observations. The results indicate that the asphalt has a crown near the middle of the surface and slopes down near the edges, as expected for what is essentially a service road leading to one of the science buildings on our campus. The procedure for determining intrinsic and cable timing difference is detailed in Paper I; the basic method is to illuminate a single detector in the lab with a lamp and then split the signal cable so that two channels of the timing correlator receive the same photon stream. By using different combinations of channels and cables, we can derive the delays for each cable and channel relative to each other. There could also be optical path length differences on the order of a few millimeters since each telescope is manufactured separately and they are therefore not exactly identical; however, we find that these are not large enough to change the location of the correlation peak when binning the data in 64-ps intervals. One centimeter of optical path delay represents a timing difference of only 33 ps, which is typically about half the length of the timing bin size we use for cross-correlations; however, we will return to this point in the analysis of the data presented later in the paper.

2.2. Data Reduction Methodology

For three-telescope work, much of our data reduction methodology remains the same as described in Paper I, where the data presented were solely from a two-telescope arrangement that was oriented in a north-south baseline. Timing cross-correlations are computed for each 5-minute sequence recorded. However, cross-correlation peaks shift position as an observation proceeds, and so to combine those properly, one must take account of where the peak in a given cross-correlation is expected to appear as a function of time, based on sky position of the target and the baseline.

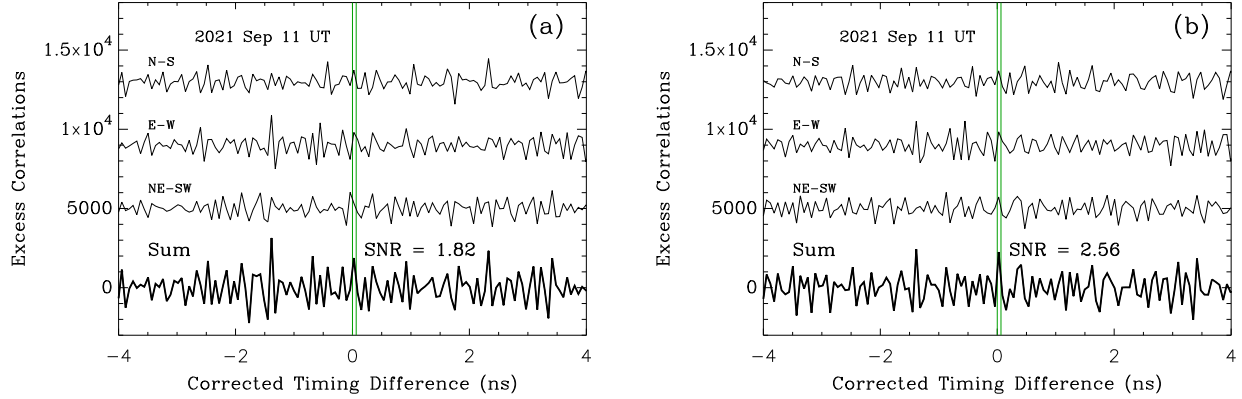


Figure 1. The cross-correlation results for each baseline on 11 Sep 2021. (a) In this case, the plots are made assuming the nominal position angles for the baselines (i.e. N-S = 180° , E-W = 90° , and NE-SW = the angle implied by completing the triangle with this baseline as the hypotenuse). (b) The same data, but using the method described in the text for accounting for position angle offsets. In each plot, the data for the individual baselines are offset from the $y = 0$ line for clarity and the vertical green lines indicate the location of the expected cross-correlation peak.

Even within a 5-minute file, small shifts occur. Our cross-correlation routine accounts for these and corrects all timing differences to the value expected at the start of the file, but leaves the peak position otherwise unchanged. When sequentially recorded files are combined, the shift value at the start of the file is computed, and that location is shifted to a nominal “zero” position in each case. Thus, when adding files, the peak builds up in a common location, defined to be zero delay. In practice, this zero position is in fact the middle of the zero bin for 64-ps binning in time; in other words, it is 32 ps from true coincidence, so that, when the data are binned down to 64-ps intervals, all of the correlations can be expected to be in the “zero” timing difference sample, which extends from 0 to 63 ps.

An important part of the analysis of the data presented in Paper I was the correction made because of presumed slight differences in the baseline orientation of the telescopes from night to night. This is done by taking the final combined cross-correlation for a given night and recomputing it with baseline orientations sweeping through a small range near the nominal position angle value of the baseline. If the peak is enhanced through this process, it is assumed that the actual placement of the telescopes was not exactly the north-south orientation we attempted to achieve but deviated from that slightly, usually no more than 0.1 to 0.2 degrees. In Paper I we show through simulation that this process results in peak values that more nearly reach the theoretical value, whereas if this is not done, SNR is sacrificed.

The addition of a third telescope creates additional complexity in the data reduction process, but also presents an opportunity for additional constraints to be applied. Our approach is as follows. We compute cross-correlations for each pair of telescopes, resulting in three different summed cross-correlations from the data for a given night. We then do the angle correction, but subject to the constraint that the three telescopes must form a triangle; that is, the three interior angles created by the baselines must sum to 180 degrees. We enforce this constraint by allowing the north-south and east-west baselines to independently vary, but constrain the third baseline (between Telescopes 2 and 3) based on the other two angles. For a source where a peak is expected, we combine all three cross-correlations and vary over this two-dimensional parameter space to determine the final angles. The final pair of angles is the closest local maximum to the nominal set of baselines. Figure 1 gives an example of the cross-correlations before and after this process for one night of data.

2.3. Three-Telescope Observations and Results

We present in this section the results of five observing sessions of Vega in three-telescope mode, together with three nights of observations of the star in two-telescope mode taken on nights where we also observed Arcturus, as discussed in the next section. Table 1 details these observations, which in all cases were taken at baselines that were small enough that Vega would be unresolved, and the cross-correlation peak representing the HBT effect would be effectively maximized. This allows us to build up that peak as efficiently as possible, and to make a comparison between our results here with those presented in Paper I on the same star observed in two-telescope mode. This is especially important because, although the amount of time spent taking data on the star each night can be as long as three hours or more, it was more typically about one hour. Our long set-up procedure prior to science observations often limits our

Table 1. New SCSI Observations of Vega.

Date (UT)	No. of Telescopes ^a	N-S Sep. (m)	E-W Sep. (m)	NE-SW Sep. (m)	Total Observing Time (hr) ^b	Avg. Count Rate per Tel. (MHz)
2021 Aug 25	3	2.529	2.651	3.664	0.42	0.150
2021 Sep 04	3	2.485	2.783	3.731	2.25	0.345
2021 Sep 11	3	2.454	2.452	3.469	3.34	0.709
2022 Jun 29	3	2.528	2.388	3.478	1.00	0.211
2025 May 12	2	2.151	—	—	1.17	0.878
2025 May 27	2	2.224	—	—	0.92	1.311
2025 Jun 04	2	2.061	—	—	2.08	0.625
2025 Jun 25	3	3.403	2.955	4.507	1.41	0.098

^a All observations taken with a filter with center wavelength of 532 nm and FWHM of 1.2 nm.

^b There are 8.42 hours of 3-telescope observations, 3.45 hours of 2-telescope observations, or 11.87 total hours of data obtained on the eight nights represented here.

ability to begin data-taking at the start of the night, and the end point of the observation sequence can be cut short by factors such as (1) the daytime obligations of observing team members, (2) losing the star as it transits the meridian due to the difficulty of manually guiding near the zenith, where the tracking of our altitude-azimuth telescopes is poor, and (3) the maritime climate in New Haven, where high fog and patchy clouds can sometimes appear unpredictably.

Figure 2 shows the final cross-correlations obtained for each of the eight nights in Table 1. The initial timing differences between stations based on the starting sky position of the star were subtracted, and then the timing differences throughout the observing session were referenced to that fiducial, so that the cross-correlation peak in each case is expected to be in the center of the timing bin at zero nanoseconds. While it is more typical to plot a version of the HBT peak from cross-correlation data that is normalized by the mean number of correlations per timing bin, the eight plots here are shown on the same “raw” scale of excess correlations, that is, the number of correlations detected in each timing bin after subtracting the average number. This highlights the variation in observing efficiency, with some nights producing better results than others. In the current analysis, we found this useful for comparing to and combining with results in Paper I, but for future science observations, we plan to adopt the standard normalization as other groups have. Figure 3 shows the signal-to-noise ratio (SNR) obtained as a function of the square root of the mean number of correlations per timing bin. We expect that, at constant count rate, the mean number of correlations will be proportional to t , the observation time. Since the SNR will scale as \sqrt{t} , the plot of SNR as a function of the square root of the mean number of correlations is expected to be linear. Fitting a line with intercept zero to the eight points representing the new data on Vega presented here, we obtain a slope of $m = 0.00269 \pm 0.00065$, which is slightly higher than the value obtained in Paper I, although still within the uncertainty.

Figure 4 shows the final result for Vega in two ways. In Figure 4(a), the timing difference data between channels are binned in 16-ps intervals, and the data show a peak in the expected location. We fitted this peak with a Gaussian function where the height and location in time were allowed to vary, but the width was fixed. As discussed in Paper I, we expect the FWHM in timing resolution for our system to be 48 ps, given the properties of our SPAD detectors, and so this is the fixed value used in the Gaussian fitting procedure. The result is shown with the red dashed curve in the figure; the height is at an excess correlation value of 1821 ± 484 and timing offset of 23 ± 8 ps. Integrating the Gaussian, a total number of excess correlations of 5815 ± 1544 is obtained. In the case of 64-ps binning, a delta-function peak is expected at the final corrected timing difference between the channels because the timing jitter of the detectors is lower than that width. In Figure 4(b), a total of 5495 excess correlations were seen from the summed data set described in Table 1, whereas the noise (*i.e.*, the standard deviation) of values to the left and right of the peak in Figure 3(b) is 1163. This is a formal significance of 4.73σ . Given that some of the average count rates shown in Table 1 are clearly lower than what can be detected with the system under good conditions, further refinements in our observing

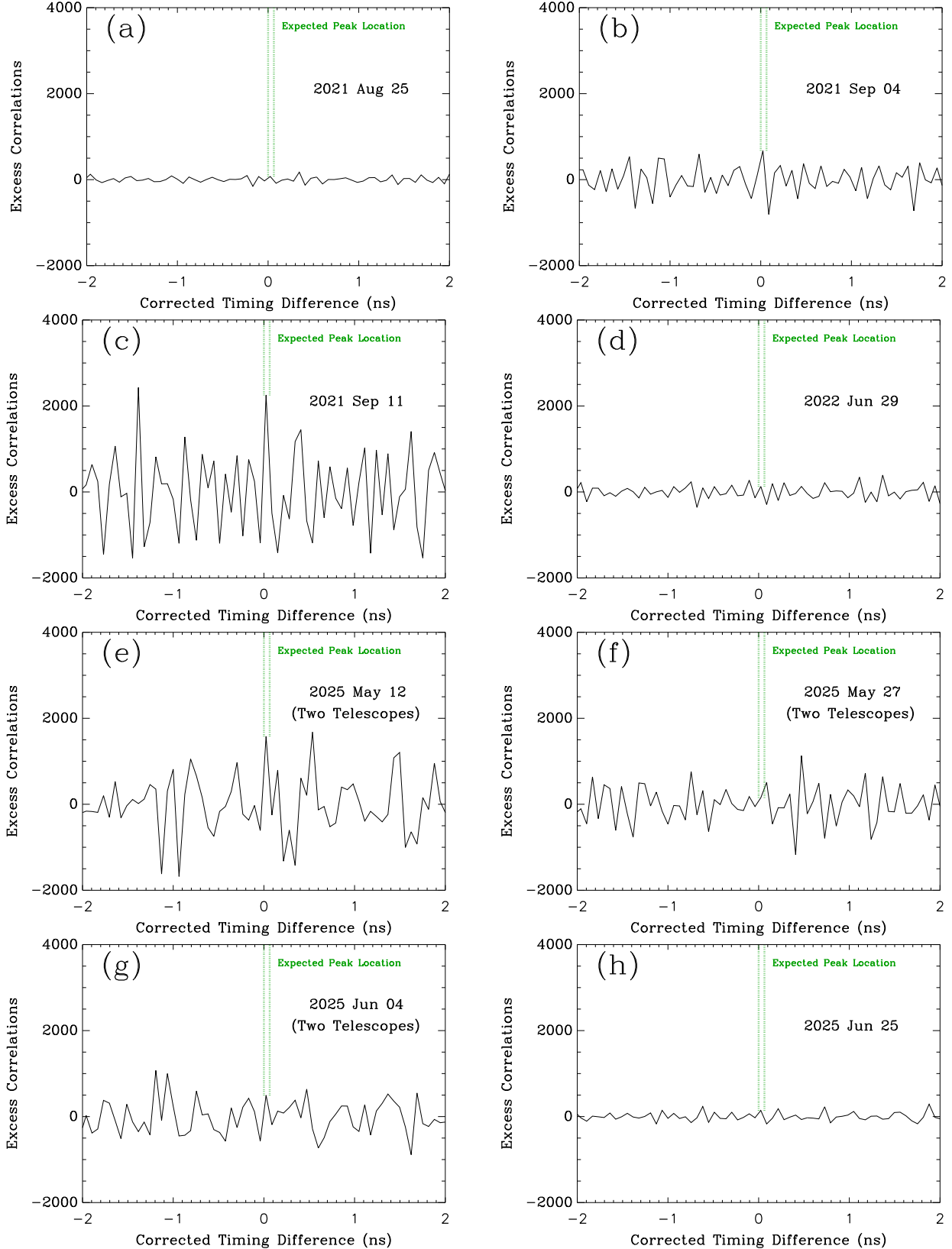


Figure 2. Cross-correlations obtained for each night listed in Table 1. In each case, the mean number of correlations per timing bin has been subtracted so that the HBT peak is more visible, and the green dotted lines mark the expected location of the peak. Except where otherwise noted, the three-telescope arrangement discussed in the text was used.

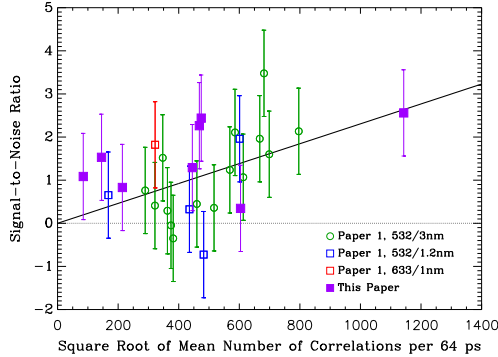


Figure 3. Signal-to-noise ratio obtained in the final cross-correlation function in each observing session listed in Table 1 as a function of the square root of the mean number of correlations obtained in a 64-ps timing bin. The filled purple squares indicate the results for the new observations presented in Table 1, all of which were with the 532/1.2 nm filters. For comparison, open symbols indicate data from Paper 1, where the filter parameters are given in the legend. A line of best fit for all data to date is shown as the solid line, and the dotted line at zero is present to guide the eye.

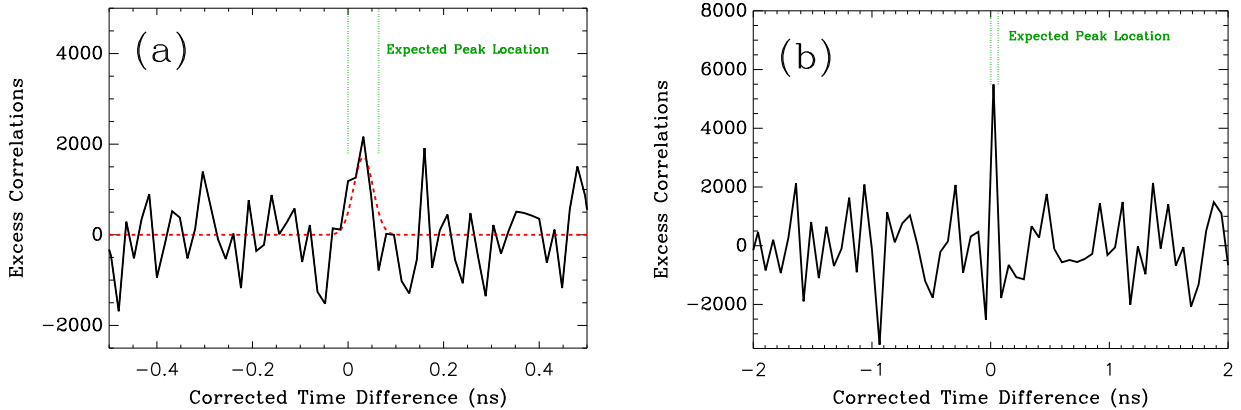


Figure 4. Cross-correlation results obtained on Vega for the entire new data set presented here. (a) In this case, the plots are made binning the timing differences between photon pairs in 16-ps bins. The black solid curve is the data, the red dashed curve is a Gaussian fit to the data, and the green dotted lines indicate the expected location of the peak based on timing corrections made throughout the dataset. (b) The same data, but using a bin width of 64 ps.

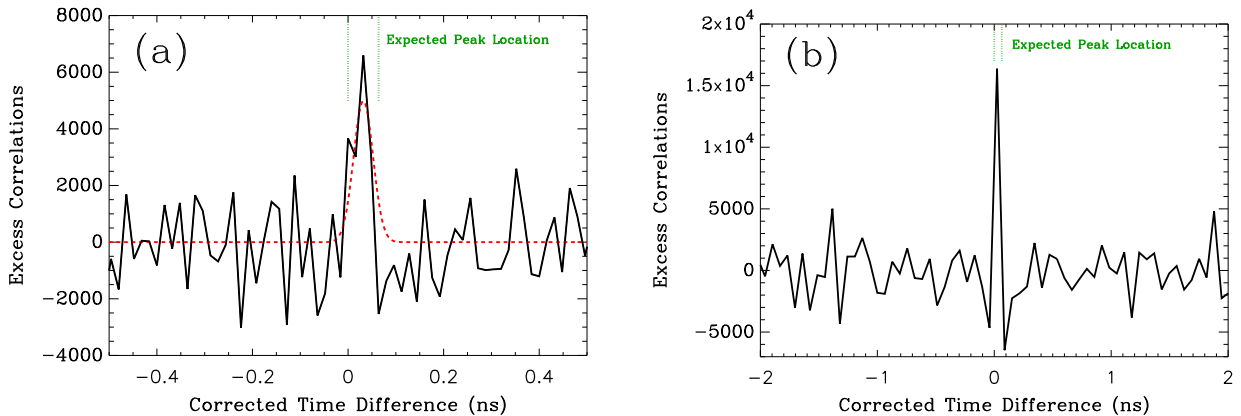


Figure 5. Cross-correlation results obtained on unresolved sources with SCSI to date by combining the results in Figure 4 with those from Paper I. (a) In this case, the plots are made binning the timing differences between photon pairs in 16-ps bins. The black solid curve is the data, the red dashed curve is a Gaussian fit to the data, and the green dotted lines indicate the expected location of the peak based on timing corrections made throughout the dataset. (b) The same data, but using a bin width of 64 ps.

procedures to reliably maximize count rates will likely continue to help us improve our ability to reach statistically significant results in a shorter amount of time.

Finally, we combine this result with that shown in Paper I, in order to update our instrumental efficiency for unresolved sources. It is important to obtain as precise a number as possible for the expected correlations when a source is unresolved prior to interpreting data from a partially-resolved star as we will do in the next section. The results are shown in Figure 5 for both the 16- and 64-ps binning. For 16-ps binning, we again fit with a Gaussian peak of fixed FWHM at 48 ps, and we find a peak value of 5193 ± 595 correlations, and the peak position sits at 25 ± 3 ps from the origin. Integrating the Gaussian, we obtain the total number of excess correlations is 16582 ± 1901 , a formal significance of 8.72σ . For 64-ps binning, we obtain 16375 excess correlations with a noise value of 1797 on either side of the peak, a formal significance of 9.11σ . As this result is obtained with mean number of correlations of 7.478×10^6 per 64-ps bin, the implied correlation efficiency of the instrument is $0.2190 \pm 0.0240\%$. This is the value we will use in the next section to represent SCSI's HBT signal for an unresolved source.

3. OBSERVATIONS OF ARCTURUS

3.1. *Observations with SCSI*

We now turn to our observations of Arcturus (= HR 5340 = HIP 69673), where in all cases we observed the star in two-telescope mode using a north-south baseline. In Paper I, observations of Arcturus that were obtained on four nights were presented, but they represented only 3.35 hours of data. While those data show that the level of correlation detected was lower than that of Vega and Deneb (which were both unresolved at the baselines used), it was not possible to use the measurement to conclude anything other than a rough lower limit on the diameter of the star. In the first half of 2025, we sought to continue observing this star with SCSI to decrease the uncertainty of the previous measure. The list of these observations is presented in Table 2. We also were able to re-analyze one night of Arcturus data that occurred on 2017 June 21 and was not presented in Paper I; this was carried out before we obtained the narrower ($\Delta\lambda = 1.2$ nm) filters that are currently used in SCSI; nonetheless, we include it here for completeness. The dataset represents ~ 8 hours of observations at an average count rate of ~ 1 MHz. Combined with the earlier dataset from Paper I, 11 hours of data on the star have now been recorded, comparable to the new dataset presented of Vega in the previous section.

We present the data in the same way as for Vega. The cross-correlation functions obtained on each night of new data are shown in Figure 6, and the SNR obtained in each case is shown in Figure 7 as a function of the square root of the mean number of correlations obtained per 64-ps timing bin. In this plot, we also include points for the 4 nights reported in Paper I. Fitting all of the data with a linear function with zero intercept, we obtain a slope of $m = 0.00118 \pm 0.00070$, or about half of the value obtained for Vega discussed in the previous section, suggesting partial correlation. Figure 8 shows the summed cross-correlation plot for the new data, at both (a) 16-ps and (b) 64-ps resolution. In the former case, a Gaussian of 48 ps is again fitted to the data, and the peak position falls closer to the high edge of the expected range in timing difference (that is, at ~ 50 ps instead of exactly in the middle of the 0-63 ps interval). One difference from the Vega data presented earlier and also two-telescope data from Paper I is that we most often used Telescope 3 in place of Telescope 2 as the northern station. Thus, if the focal length of Telescope 3 is slightly different from Telescope 2, changing the optical path length by a few millimeters, this could explain such a shift. Figure 9 is the same as Figure 8, but includes the Arcturus data from Paper I in the summations (and we make no correction for the slight offset just mentioned). These plots appear very similar to Figure 8 due to the fact that the combined dataset is dominated by the new observations; nonetheless, we include the older data as it provides an incremental increase in the SNR overall.

For Figure 8, we obtain a peak value at 16-ps binning that has value 1247 ± 454 , with the position of the peak at 54.4 ± 10.5 ps. The integral of the fit, representing the total number of excess correlations is 3980 ± 1449 . For the 64-ps binning shown in Figure 8(b), we have a measured signal in the expected timing bin of 2390 counts, with the standard deviation of values on either side of this location being 1321. This implies a SNR of 1.810, with the mean number of correlations per 64-ps bin being 2.02×10^6 counts.

In Figure 9, we combine these results with those presented in Paper I. Here, for 16-ps binning and fitting in the same way as for Vega, we obtain a peak value of 1258 ± 476 at 56.3 ± 10.9 ps. The integral of the fit implies a total of 4018 ± 1520 excess counts. For 64-ps binning, we obtain an excess of 2603 counts in the expected timing bin, with a standard deviation of 1370 counts. Thus, the SNR here is 1.90 after having obtained 2.42×10^6 correlations per 64-ps bin in the summation of all files. In both the case of Vega and Arcturus, the results of binning at 16 ps show

Table 2. New SCSI Observations of Arcturus

Date (UT)	N-S Sep. (m)	Total Observing Time (hr) ^a	Avg. Count Rate per Tel. (MHz)
2017 Jun 21 ^b	2.331	0.33	0.272
2025 Apr 18	3.005	0.48	1.333
2025 Apr 25	2.359	1.27	1.197
2025 May 01	2.129	1.25	1.314
2025 May 12	2.151	1.11	0.770
2025 May 27	2.224	1.75	1.165
2025 Jun 04	2.061	1.58	0.546

^aThere are 7.77 total hours of data obtained on the seven nights represented here.

^bThis observation taken with the $\lambda/\Delta\lambda = 532/3.0$ filter.

that we do not miss a significant number of counts by binning the correlations by 64 ps, nor do we increase the noise. It is therefore reasonable in what follows here to use only the results binned at 64 ps. More sophisticated analyses using higher timing resolution may be possible, but it is unlikely that they would dramatically increase the statistical significance of the results over this simple and straightforward approach.

The data presented allow us to estimate the squared visibility of Arcturus for the baseline of our observations. Dividing the excess correlations by the mean number of correlations per 64-ps bin, we obtain $0.107 \pm 0.056\%$, which represents the percentage of intensity-correlated photons detected. For unpolarized light, the relationship between the cross-correlation results and the complex visibility function of the source is expected to be

$$g_{\text{unpol}}^{(2)} = 1 + \frac{1}{2}|V_{12}|^2 \frac{\Delta\tau}{\Delta t}, \quad (1)$$

where $g_{\text{unpol}}^{(2)}$ is the cross-correlation function in the case where the mean number of correlations per timing bin is normalized to 1, $|V_{12}|^2$ is the squared visibility, $\Delta\tau$ is the timescale of intensity fluctuations set by the frequency bandwidth of the system, and Δt is the timing resolution used. The measurements of excess correlation discussed here effectively subtract the 1 on the right side of the equation and are represented by the second term on the right; thus, to obtain the visibility measurement for Arcturus, we divide the correlation percentage obtained for Arcturus by that of Vega from the previous section. The final result is $|V_{12}|^2 = 0.49 \pm 0.26$. The range of spatial frequencies to which this result applies will be discussed in Section 4.

3.2. Speckle Imaging of Arcturus

In June of 2025, three of us (E.P.H., J.W.D., and S.R.M.) had the opportunity to observe Arcturus using speckle imaging at the ARC 3.5-m Telescope located at Apache Point Observatory (APO) in New Mexico. The instrument used for these observations was the Differential Speckle Survey Instrument (DSSI) (E. P. Horch et al. 2009). As detailed in E. P. Horch et al. (2023) and J. W. Davidson et al. (2024), DSSI was moved from its previous home at Lowell Observatory to APO in early 2022, and since that time Southern Connecticut State University has collaborated with the University of Virginia to build a long-term speckle program there.

Arcturus was observed on two nights, 08 and 11 June 2025 UT. In both cases, 3000 1-ms frames were taken of the star, followed by 3000 1-ms frames taken of a bright unresolved star, HR 5405 (HD 126661, 22 Boo). HR 5405 is a late A or early F giant (R. O. Gray et al. 2001) at a distance of 96 pc, so its inferred diameter based on stellar properties is $4.03 \pm 0.25 R_\odot$ (Gaia Collaboration et al. 2018), and therefore the angular diameter is approximately 0.39 mas, which is sufficiently small to be considered as completely unresolved for our purposes, given that Arcturus is partially resolved over a baseline of 2-3 meters, as shown in the previous section. DSSI collects data in two filters simultaneously; in our case, those filters were a red ($\lambda_0 = 692$ nm, $\Delta\lambda = 40$ nm) and near infrared ($\lambda_0 = 880$ nm, $\Delta\lambda = 50$ nm). The seeing measured on both nights was between 0.8 and 1 arcsecond.

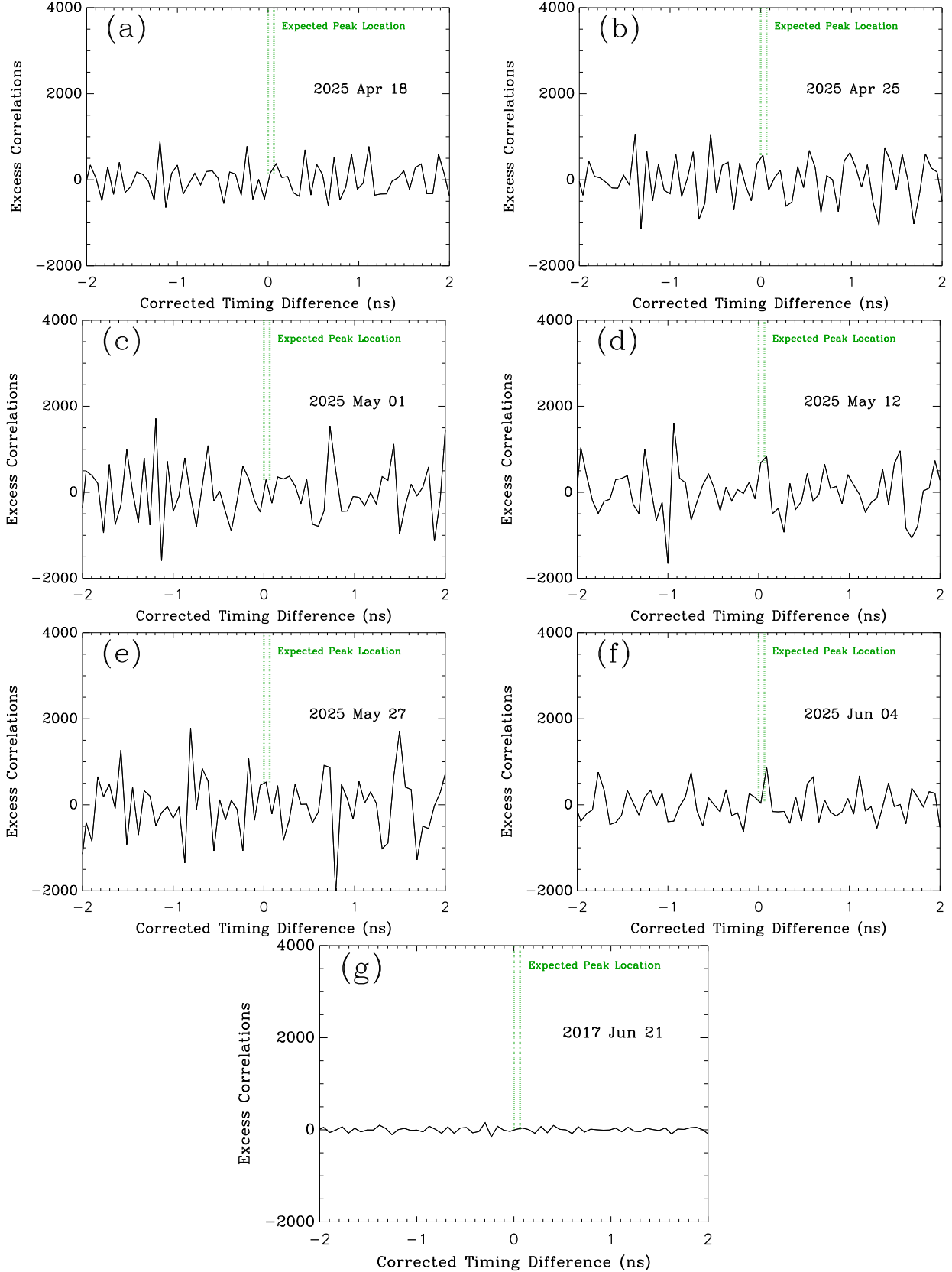


Figure 6. Cross-correlations obtained for each night listed in Table 2. In each case, the mean number of correlations per timing bin has been subtracted so that the HBT peak is more visible, and the green dotted lines mark the expected location of the peak. The two-telescope arrangement discussed in the text was used for all observations here.

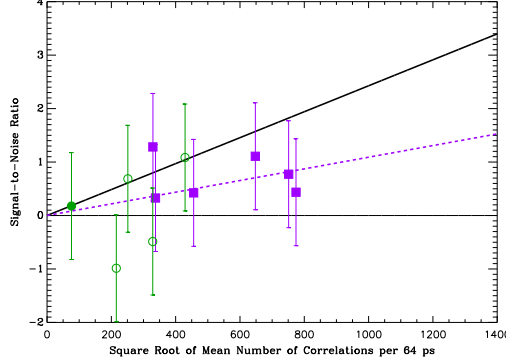


Figure 7. Signal-to-noise ratio obtained in the final cross-correlation function in each observing session listed in Table 2 as a function of the square root of the mean number of correlations obtained in a 64-ps timing bin. The purple squares indicate the results from Table 2, except for the 2017 Jun 21 data, which is shown as a solid green circle. For comparison, we also include here the data from Paper I as open green circles. Both the 2017 Jun 21 data and the Paper I data were obtained with a filter of center wavelength/FWHM of $\lambda/\Delta\lambda = 532/3\text{nm}$. The line of best fit from Figure 3 is shown as the solid line, the dashed purple line indicates the line of best fit for Arcturus, and the solid line at zero is present to guide the eye.

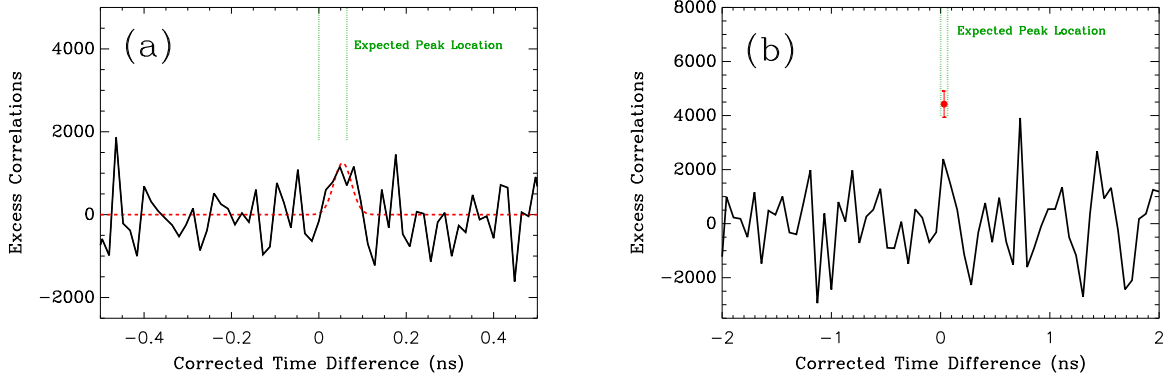


Figure 8. Cross-correlation results obtained on Arcturus for the new data set presented here. (a) In this case, the plots are made binning the timing differences between photon pairs in 16-ps bins. The black solid curve is the data, the red dashed curve is a Gaussian fit to the data, and the green dotted lines indicate the expected location of the peak based on timing corrections made throughout the dataset. (b) The same data, but using a bin width of 64 ps. The red filled circle indicates the signal value expected for full correlation based on the results from Vega in the previous section.

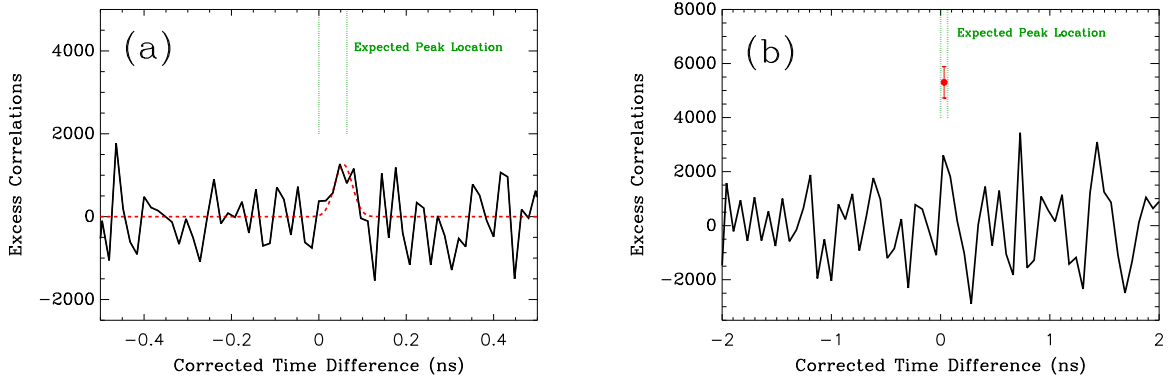


Figure 9. Cross-correlation results obtained on Arcturus for the data set presented here plus the results in Paper I. (a) In this case, the plots are made binning the timing differences between photon pairs in 16-ps bins. The black solid curve is the data, the red dashed curve is a Gaussian fit to the data, and the green dotted lines indicate the expected location of the peak based on timing corrections made throughout the dataset. (b) The same data, but using a bin width of 64 ps. The red filled circle indicates the signal value expected for full correlation based on the results from Vega in the previous section.

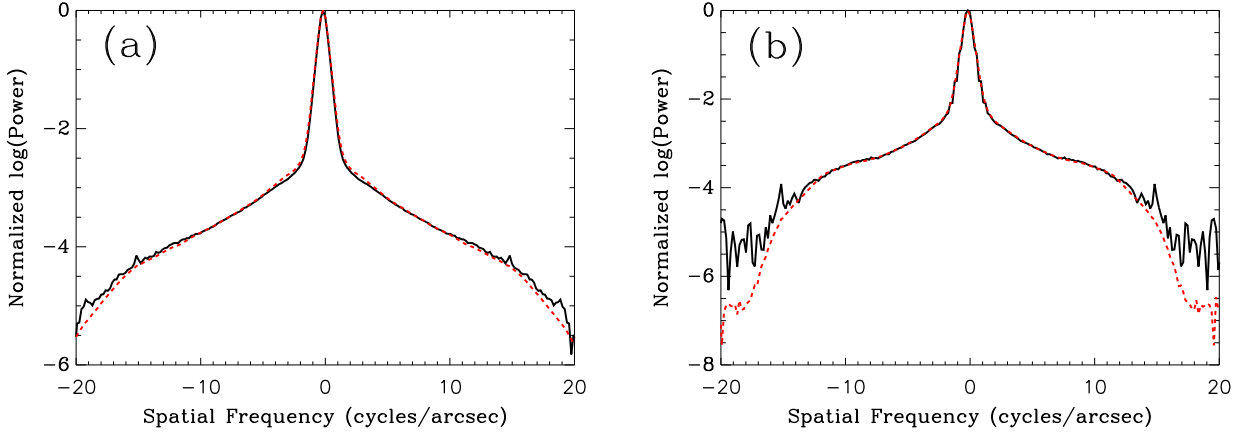


Figure 10. A cross section of the two-dimensional power spectrum obtained using speckle imaging. (a) The result at 692 nm. (b) The result at 880 nm. In both plots, the solid line is the power spectrum of the unresolved star, HR 5405, and the red dashed curve is the power spectrum of Arcturus. The large peak at low frequencies is caused by seeing, and in both cases, the curves are nearly identical at lower spatial frequencies, but begin to slightly diverge at the higher frequencies shown, with Arcturus having lower power in that region. Note that the curves do not extend to as high a limit for the 880-nm data because the diffraction limit is reached at a lower spatial frequency for the longer wavelength. A higher noise floor is also seen above the diffraction limit for the point source at 880-nm because it is a fainter star than Arcturus.

The reduction of the speckle frames follows the standard autocorrelation analysis that has been described in e.g. [J. W. Davidson et al. \(2024\)](#) and other papers. The basic process is to debias frames and compute their autocorrelations, and then sum the autocorrelations for the entire sequence. This retains diffraction-limited information. Completing the same steps for the point source observations, we can then deconvolve the speckle transfer function from the data on Arcturus by moving to the Fourier domain and dividing. A comparison of the Fourier transform of both Arcturus' autocorrelation (which is equivalent to its spatial frequency power spectrum) and that of the point source is shown for each filter in Figure 10. It is seen that at higher spatial frequencies, there is a small but statistically significant loss of power in the Arcturus data relative to that of HR 5405, indicating that, while Arcturus' angular diameter is below the diffraction limit at the ARC telescope, there is a partial resolution of the star at the highest spatial frequencies represented.

4. A NEW MEASUREMENT OF THE DIAMETER OF ARCTURUS

By combining the data from both SCSI and DSSI, we are in a position to measure the visibility function of Arcturus. The spatial frequency power spectrum of the star, once deconvolved by that of the point source HR 5405 and normalized, yields the 2-D squared visibility at low spatial frequencies. The intensity interferometry data supplement our information at higher spatial frequencies. To help visualize the information we have, Figure 11(a) shows the spatial frequency coverage of our data, where we have considered only spatial frequencies up to 16 cycles/arcsec for the speckle imaging data in order to maintain high signal-to-noise results. In Figure 11(b), we radially average the data to obtain a visibility curve as a function of spatial frequency. In the case of the speckle data, we use annuli of width 2 pixels in the frequency domain centered on spatial frequencies of 2, 4, 6, ..., and 18 cycles per arcsecond for 692-nm speckle data, and 2, 4, 6, ..., and 12 cycles per arcsecond for the 880-nm speckle data. We do this for each filter on both nights, generating four independent estimates of the squared visibility for these frequencies. Individual results of each observing session with SCSI are then also plotted, along with the average value presented in the previous section.

Figure 11 also plots the best fit to the data for a radially-symmetric limb-darkened profile. As discussed in [E. K. Baines et al. \(2018\)](#), if $x = \pi B \theta_{LD} \lambda^{-1}$ where B is the baseline, θ_{LD} is the limb-darkened stellar diameter, and λ is the observation wavelength, then one may model the visibility squared for a limb-darkened disk as

$$V^2 = \left(\frac{1-\mu}{2} + \frac{\mu}{3} \right)^{-1} \times \left[(1-\mu) \frac{J_1(x)}{x} + \mu \left(\frac{\pi}{2} \right)^{1/2} \frac{J_{3/2}(x)}{x^{3/2}} \right]^2, \quad (2)$$

where μ is the limb darkening parameter, which is generally wavelength dependent. In our case, we have data at three different wavelengths, 692 nm and 880 nm from the speckle observations and 532 nm from the intensity interferometry observations. Baines et al. derived values for μ for a range of stellar temperatures and assuming observing in the R

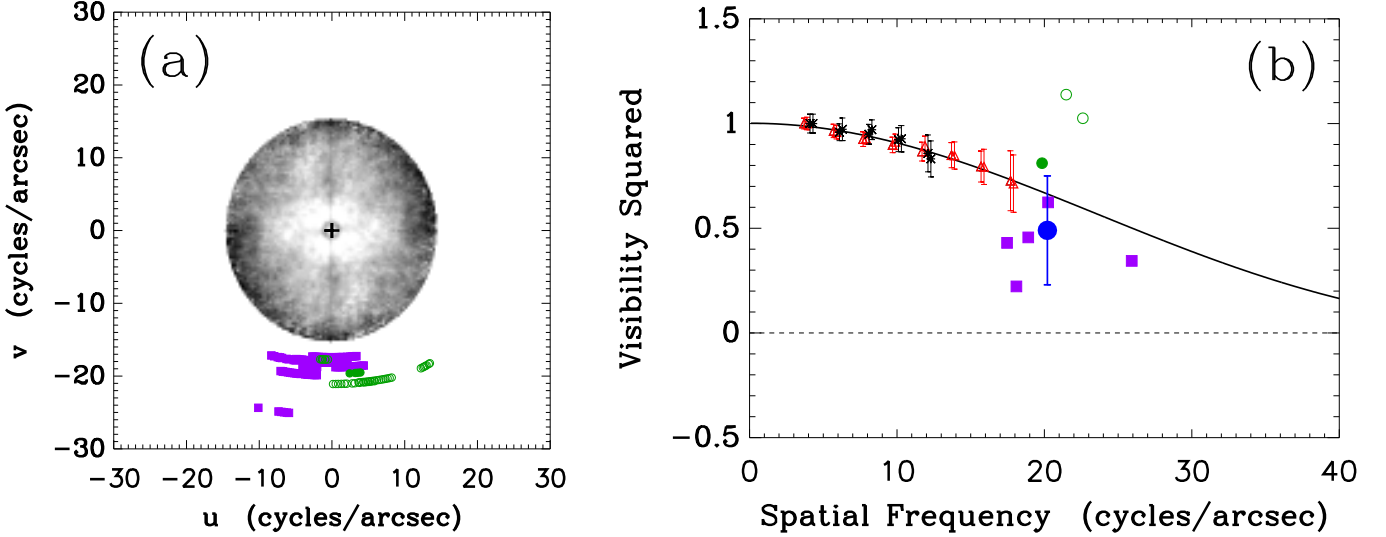


Figure 11. (a) The spatial frequency coverage for Arcturus. The grayscale image inside the circle represents the derived spatial frequency power spectrum for the averaged speckle data, extending out to 15 cycles/arcsec, with darker shades near the edge of the circle indicating lower power. The cross marks the origin in the uv -plane, and the purple and green data points illustrate the observing sessions with the intensity interferometer. The color coding and symbols are the same as in Figure 7. (b) The visibility curve for Arcturus. Here, the red triangles are the radially averaged values of visibility for the 692-nm speckle data, the asterisk symbols are the 880-nm speckle data, and the blue filled circle is the summed result for the intensity interferometry data. Green and purple squares indicate the visibilities obtained for individual observing sessions, albeit with large uncertainty in each case. The colors and symbols are the same as in Figure 7, and three observations included in the final visibility measure fall outside the plot window. The solid curve is the fitted visibility as a function of spatial frequency, and the dashed curve is drawn at zero to guide the eye.

band; generally, for stars with similar temperatures as Arcturus, the value for μ was ~ 0.8 . As our highest signal-to-noise data (692 nm) are also near the R band, with some data above and below that value, we adopt $\mu = 0.8$ for the analysis here. In principle, with more data, we could fit for μ at each wavelength, but in this study we simply fit the data to the function in Equation 2 to a two-parameter fit: θ_{LD} and an overall (arbitrary) normalization constant. To avoid systematic error due to seeing mismatch between Arcturus and the point source, we do not consider spatial frequencies below 4 cycles per arcsecond. Likewise, we only use the speckle data up to 18 cycles/arcsec at 692 nm, and up to 12 cycles per arcsec at 880 nm, since the SNR deteriorates quickly above these values. We normalize the values we have for each filter to 1 at 4 cycles per arcsec, and then perform the two-parameter fit. The result of that operation is $\theta_{LD} = 21.5 \pm 1.8$ mas, with a normalization of 1.001 ± 0.013 .

5. DISCUSSION

Several other studies exist in the literature which measure the angular diameter of Arcturus. The first direct measure was due to [F. G. Pease \(1931\)](#), and speckle interferometry contributed two measures in the 1970's using the Palomar 5-m telescope and the Kitt Peak 4-m telescope, respectively ([D. Y. Gezari et al. 1972](#); [S. P. Worden 1976](#)). While Pease did not give an uncertainty for his measure, the speckle results were stated with uncertainties of ~ 14 and $\sim 35\%$, respectively. Starting in the 1980's, a series of high-precision measures have been made using long baseline optical and infrared interferometers. [G. P. di Benedetto & R. Foy \(1986\)](#) presented a measurement using the I2T interferometer at CERGA Observatory in France. The observations were made in three filters centered near 2.2 microns but having different widths, using baselines of 18-34 m. [G. Perrin et al. \(1998\)](#), [T. Verhoelst et al. \(2005\)](#), and [S. Lacour et al. \(2008\)](#) present measures using IOTA (Mt. Hopkins, Arizona) that span over a decade, taken in the K -band (2.2 microns) for the first two studies, and then the H -band (1.6 microns) for the third result. A result using the Mark III Optical Interferometer is given in [A. Quirrenbach et al. \(1996\)](#), while [D. Mozurkewich et al. \(2003\)](#) detail a measurement using the Navy Precision Optical Interferometer. These were both done at several visible wavelengths (between 450 and 800nm) using baselines of less than 10 m. [A. Richichi et al. \(2009\)](#) provide a measurement using VINCI at VLTI, where the observations were performed at the K -band. Finally, [K. Ohnaka & C. A. L. Morales Marín \(2018\)](#) used the AMBER instrument at VLTI to spatially resolve the star in individual CO line wavelengths, finding evidence for a cool component extending out to 2-3 times the radius of the star.

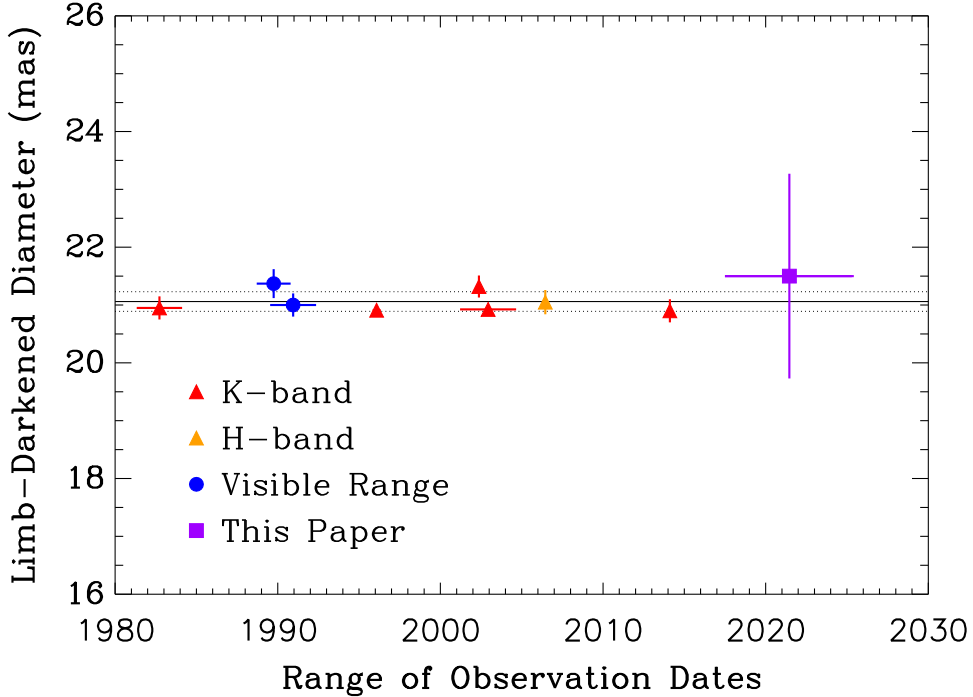


Figure 12. Diameter measurements of Arcturus made by various groups since 1980 using interferometric techniques. *K*-band measures are from I2T, IOTA, and VLTI, the *H*-band data point is from IOTA, the visible measures are made by the Mark III interferometer and NPOI, and the purple square indicates the measure presented here. Vertical error bars are included for all measures, and the horizontal error bars indicate the timeframe over which the observations were taken in each case. For our measure, though the timeline extends from our earliest observations in 2017 to the present, most of the data are from 2025. The black solid and dotted lines indicate the weighted average and uncertainty found in [I. Ramírez & C. Allende Prieto \(2011\)](#), 21.06 ± 0.17 mas.

[I. Ramírez & C. Allende Prieto \(2011\)](#) provided a summary of diameter measurements made of Arcturus from the 1980's through 2011, where they corrected measurements for limb-darkening if the original work had not done so, and they derive a final weighted diameter of 21.06 ± 0.17 mas. [K. Ohnaka & C. A. L. Morales Marín \(2018\)](#) came after that paper, and they gave a uniform disk diameter of 20.4 ± 0.2 mas for the CO continuum at 2.3 microns. Following [I. Ramírez & C. Allende Prieto \(2011\)](#), we estimate that this value underestimates the limb-darkened diameter by approximately 0.5 mas at 2.3 microns, leading to a limb-darkened value of 20.9 ± 0.2 mas.

In Figure 12, we show the long baseline optical interferometry measurements mentioned above together with our own measure. (That is, we exclude the 1931 result of Pease and the early speckle results.) While results from the Michelson interferometers show higher precision than the result from SCSI presented here, repeating the measurement, especially with a technique in the visible that differs from visible-light Michelson interferometers like the Mark III or NPOI, is useful. Ironically, most of the other modern intensity interferometers that have produced diameter measurements of stars in the last few years do not have the capability of observing at small enough baselines to detect the HBT signal from Arcturus. Taken as a whole, the diameter measures in Figure 12 show consistency through the years, across a factor of more than 4 in wavelength, and, now, with our result, between the two techniques represented (Michelson interferometry and intensity interferometry). Further observations in 3-telescope mode with SCSI will of course help us reduce the uncertainties in the intensity interferometry result.

6. CONCLUSIONS

We have presented our second large set of observations using the Southern Connecticut Stellar Interferometer (SCSI). In the first group of observations presented here, we used SCSI in a three-telescope mode for the first time. We observed Vega, producing a nearly 5σ photon bunching peak in roughly 12 hours on sky. This allowed us to combine with the results from our first paper to update the fraction of correlated photons seen with our instrument to $0.2190 \pm 0.0240\%$. In the spring of 2025, we were then able to observe Arcturus on 6 nights, finding a reduced fraction of correlated photons in that case. Forming the ratio of these two correlation percentage allowed us to measure the squared visibility of Arcturus at spatial frequencies near 20 cycles/arcsec as 0.49 ± 0.26 . In combination with speckle data

taken with the DSSI speckle camera at the ARC 3.5-m Telescope, we filled in the lower spatial frequencies for the star's visibility profile. Finally, by fitting a limb-darkened profile to the visibility curve in the Fourier domain, we obtain a diameter for Arcturus of 21.5 ± 1.8 mas. While the uncertainty is larger than the Michelson-style long baseline optical interferometers have obtained, this is the first measurement of Arcturus' diameter that incorporates some intensity interferometry data. The speckle dataset, supplemented by the SCSI result, yields a measurement that is similar in precision to other stellar diameters obtained with modern intensity interferometers to date. (We measure the diameter to 8% uncertainty.) Our measurement is also consistent with those of previously published studies on Arcturus.

ACKNOWLEDGEMENTS

We gratefully acknowledge support from the National Science Foundation in the completion of this work, specifically grants AST-1429015 and AST-1909582. We are also grateful to the Connecticut Space Grant Consortium for supporting our 2025 observing campaign with SCSI through Faculty Research Grant P-2332, and to the Board of Regents of the Connecticut State University system for a Connecticut State University Research Grant. Finally, we thank the excellent staff at Apache Point Observatory for their help in securing the speckle observations, and the anonymous referee for helpful comments during the review process.

This work presents results from the European Space Agency (ESA) space mission Gaia. Gaia data are being processed by the Gaia Data Processing and Analysis Consortium (DPAC). Funding for the DPAC is provided by national institutions, in particular the institutions participating in the Gaia MultiLateral Agreement (MLA). The Gaia mission website is <https://www.cosmos.esa.int/gaia>. The Gaia archive website is <https://archives.esac.esa.int/gaia>. We also made use of the SIMBAD database, operated at CDS, Strasbourg, France.

Facilities: APO:ARC.

REFERENCES

Abeysekara, A. U., Benbow, W., Brill, A., et al. 2020, *Nature Astronomy*, 4, 1164, doi: [10.1038/s41550-020-1143-y](https://doi.org/10.1038/s41550-020-1143-y)

Acciari, V. A., Bernardos, M. I., Colombo, E., et al. 2020, *MNRAS*, 491, 1540, doi: [10.1093/mnras/stz3171](https://doi.org/10.1093/mnras/stz3171)

Acharyya, A., Aufdenberg, J. P., Bangale, P., et al. 2024, *ApJ*, 966, 28, doi: [10.3847/1538-4357/ad2b68](https://doi.org/10.3847/1538-4357/ad2b68)

Archer, A., Aufdenberg, J. P., Bangale, P., et al. 2025, arXiv e-prints, arXiv:2506.15027, doi: [10.48550/arXiv.2506.15027](https://doi.org/10.48550/arXiv.2506.15027)

Baines, E. K., Armstrong, J. T., Schmitt, H. R., et al. 2018, *AJ*, 155, 30, doi: [10.3847/1538-3881/aa9d8b](https://doi.org/10.3847/1538-3881/aa9d8b)

Brown, R. H., & Twiss, R. Q. 1956, *Nature*, 177, 27, doi: [10.1038/177027a0](https://doi.org/10.1038/177027a0)

Brown, R. H., & Twiss, R. Q. 1958, *Proceedings of the Royal Society of London Series A*, 248, 199, doi: [10.1098/rspa.1958.0239](https://doi.org/10.1098/rspa.1958.0239)

Cortina, J., Cifuentes-Santos, A., Hassan, T., & Frias, F. 2025, arXiv e-prints, arXiv:2511.16505, doi: [10.48550/arXiv.2511.16505](https://doi.org/10.48550/arXiv.2511.16505)

Davidson, J. W., Horch, E. P., Majewski, S. R., et al. 2024, *AJ*, 167, 117, doi: [10.3847/1538-3881/ad1ff6](https://doi.org/10.3847/1538-3881/ad1ff6)

de Almeida, E. S. G., Hugbart, M., Domiciano de Souza, A., et al. 2022, *MNRAS*, 515, 1, doi: [10.1093/mnras/stac1617](https://doi.org/10.1093/mnras/stac1617)

di Benedetto, G. P., & Foy, R. 1986, *A&A*, 166, 204

Gaia Collaboration, Brown, A. G. A., Vallenari, A., et al. 2018, *A&A*, 616, A1, doi: [10.1051/0004-6361/201833051](https://doi.org/10.1051/0004-6361/201833051)

Gezari, D. Y., Labeyrie, A., & Stachnik, R. V. 1972, *ApJL*, 173, L1, doi: [10.1086/180906](https://doi.org/10.1086/180906)

Gray, R. O., Napier, M. G., & Winkler, L. I. 2001, *AJ*, 121, 2148, doi: [10.1086/319956](https://doi.org/10.1086/319956)

Hanbury Brown, R., Davis, J., & Allen, L. R. 1974, *MNRAS*, 167, 121, doi: [10.1093/mnras/167.1.121](https://doi.org/10.1093/mnras/167.1.121)

Horch, E. P., Davidson, Jr., J. W., Majewski, S. R., et al. 2023, in *American Astronomical Society Meeting Abstracts*, Vol. 241, American Astronomical Society Meeting Abstracts #241, 305.06

Horch, E. P., Veillette, D. R., Baena Gallé, R., et al. 2009, *AJ*, 137, 5057, doi: [10.1088/0004-6256/137/6/5057](https://doi.org/10.1088/0004-6256/137/6/5057)

Horch, E. P., Weiss, S. A., Klaucke, P. M., Pellegrino, R. A., & Rupert, J. D. 2022, *AJ*, 163, 92, doi: [10.3847/1538-3881/ac43bb](https://doi.org/10.3847/1538-3881/ac43bb)

Karl, S., Leopold, V. G., Richter, S., et al. 2025, in *Society of Photo-Optical Instrumentation Engineers (SPIE) Conference Series*, Vol. 13448, *Advanced Photon Counting Techniques XIX*, ed. M. A. Itzler, J. C. Bienfang, & K. A. McIntosh, 1344802, doi: [10.1117/12.3056039](https://doi.org/10.1117/12.3056039)

Lacour, S., Meimon, S., Thiébaut, E., et al. 2008, *A&A*, 485, 561, doi: [10.1051/0004-6361:200809611](https://doi.org/10.1051/0004-6361:200809611)

Leopold, V. G., Karl, S., Rivet, J.-P., & von Zanthier, J. 2025, *Journal of Astronomical Telescopes, Instruments, and Systems*, 11, 035005, doi: [10.1111/1.JATIS.11.3.035005](https://doi.org/10.1111/1.JATIS.11.3.035005)

Matthews, N., Gori, P. M., & Vakili, F. 2025, *MNRAS*, 538, 867, doi: [10.1093/mnras/staf249](https://doi.org/10.1093/mnras/staf249)

Matthews, N., Rivet, J.-P., Vernet, D., et al. 2023, *AJ*, 165, 117, doi: [10.3847/1538-3881/acb142](https://doi.org/10.3847/1538-3881/acb142)

Mozdzen, T. J., Scott, R. M., Mauskopf, P. D., & Rodriguez, R. R. 2025, *MNRAS*, 537, 2527, doi: [10.1093/mnras/staf226](https://doi.org/10.1093/mnras/staf226)

Mozurkewich, D., Armstrong, J. T., Hindsley, R. B., et al. 2003, *AJ*, 126, 2502, doi: [10.1086/378596](https://doi.org/10.1086/378596)

Ohnaka, K., & Morales Marín, C. A. L. 2018, *A&A*, 620, A23, doi: [10.1051/0004-6361/201833745](https://doi.org/10.1051/0004-6361/201833745)

Pease, F. G. 1931, *Ergebnisse der exakten Naturwissenschaften*, 10, 84, doi: [10.1007/BFb0111943](https://doi.org/10.1007/BFb0111943)

Perrin, G., Coudé du Foresto, V., Ridgway, S. T., et al. 1998, *A&A*, 331, 619

Quirrenbach, A., Mozurkewich, D., Buscher, D. F., Hummel, C. A., & Armstrong, J. T. 1996, *A&A*, 312, 160

Ramírez, I., & Allende Prieto, C. 2011, *ApJ*, 743, 135, doi: [10.1088/0004-637X/743/2/135](https://doi.org/10.1088/0004-637X/743/2/135)

Richichi, A., Percheron, I., & Davis, J. 2009, *MNRAS*, 399, 399, doi: [10.1111/j.1365-2966.2009.15289.x](https://doi.org/10.1111/j.1365-2966.2009.15289.x)

Rivet, J.-P., Vakili, F., Lai, O., et al. 2018, *Experimental Astronomy*, 46, 531, doi: [10.1007/s10686-018-9595-0](https://doi.org/10.1007/s10686-018-9595-0)

Rivet, J.-P., Siciak, A., de Almeida, E. S. G., et al. 2020, *MNRAS*, 494, 218, doi: [10.1093/mnras/staa588](https://doi.org/10.1093/mnras/staa588)

Tolila, S., Labeyrie, G., Kaiser, R., Rivet, J.-P., & Guerin, W. 2024, in SF2A-2024: Proceedings of the Annual meeting of the French Society of Astronomy and Astrophysics, ed. M. Béthermin, K. Baillié, N. Lagarde, J. Malzac, R. M. Ouazzani, J. Richard, O. Venot, & A. Siebert, 197–200

Verhoelst, T., Bordé, P. J., Perrin, G., et al. 2005, *A&A*, 435, 289, doi: [10.1051/0004-6361:20042356](https://doi.org/10.1051/0004-6361:20042356)

Vogel, N., Zmija, A., Wohlleben, F., et al. 2025, *MNRAS*, 537, 2334, doi: [10.1093/mnras/stae2643](https://doi.org/10.1093/mnras/stae2643)

Worden, S. P. 1976, *PASP*, 88, 69, doi: [10.1086/129899](https://doi.org/10.1086/129899)

Zampieri, L., Naletto, G., Burtovoi, A., Fiori, M., & Barbieri, C. 2021, *MNRAS*, 506, 1585, doi: [10.1093/mnras/stab1387](https://doi.org/10.1093/mnras/stab1387)

Zmija, A., Vogel, N., Wohlleben, F., et al. 2024, *MNRAS*, 527, 12243, doi: [10.1093/mnras/stad3676](https://doi.org/10.1093/mnras/stad3676)